ARCHIVIO ISTITUZIONALE
DELLA RICERCA

Alma Mater Studiorum Università di Bologna
Archivio istituzionale della ricerca

Gold Nanostar-Decorated Electrospun Nanofibers Enable On-Demand Drug Delivery

This is the final peer-reviewed author's accepted manuscript (postprint) of the following publication:

Published Version:
Bayan, M., Kosik-Koziol, A., Krysiak, Z.j., Zakrzewska, A., Lanzi, M., Nakielski, P., et al. (2025). Gold Nanostar-Decorated Electrospun Nanofibers Enable On-Demand Drug Delivery. MACROMOLECULAR RAPID COMMUNICATIONS, 46(13), 1-10 [10.1002/marc.202500033].

Availability:
This version is available at: https://hdl.handle.net/11585/1014353 since: 2025-09-16

Published:
DOI: http://doi.org/10.1002/marc.202500033

Terms of use:

Some rights reserved. The terms and conditions for the reuse of this version of the manuscript are specified in the publishing policy. For all terms of use and more information see the publisher's website.

This item was downloaded from IRIS Università di Bologna (https://cris.unibo.it/).
When citing, please refer to the published version.

(Article begins on next page)

17 November 2026

Gold Nanostar-Decorated Electrospun Nanofibers Enable On-Demand Drug Delivery

*Mohammad Ali Haghighat Bayan, Alicja Kosik-Kozioł, Zuzanna Joanna Krysiak, Anna Zakrzewska, Massimiliano Lanzi, Paweł Nakielski, and Filippo Pierini**

M. A. Haghighat Bayan, A. Kosik-Kozioł, Z. J. Krysiak, A. Zakrzewska,

P. Nakielski, F. Pierini

Institute of Fundamental Technological Research Polish Academy of Sciences

ul. Pawin´skiego 5B, Warsaw 02-106, Poland E-mail: fpierini@ippt.pan.pl

M. Lanzi

Department of Industrial Chemistry "Toso Montanari" Alma Mater Studiorum – University of Bologna

Viale del Risorgimento 4, Bologna 40136, Italy

F. Pierini

Commonwealth Scientific and Industrial Research Organization (CSIRO) Clayton, VIC 3168, Australia

Abstract

This study explores the development of a photo-responsive bicomponent electrospun platform and its drug delivery capabilities. This platform is composed of two polymers of poly(lactide-*co*-glycolide) (PLGA) and poly(3-hydroxybutyrate-*co*-3-hydroxyvalerate) (PHBV). Then, the platform is decorated with plasmonic gold nanostars (Au NSs) that are capable of on-demand drug release. Using Rhodamine-B (RhB) as a model drug, the drug release behavior of the bi-polymer system is compared versus homopolymer fibers. The RhB is incorporated in the PHBV part of the platform, which provides a more sustained drug release, both in the absence and presence of near-infrared (NIR) irradiation. Under NIR exposure, thermal imaging reveals a notable increase in surface temperature, facilitating enhanced drug release. Furthermore, the platform demonstrates on-demand drug release upon multiple NIR irradiation cycles. This platform offers a promising approach for stimuli-responsive drug delivery, making it a strong candidate for on-demand therapy applications.

1. Introduction

In drug delivery systems, on-demand release is an approach that allows for the targeted and precise release of therapeutic agents.[1–4] In contrast to conventional sustained-release systems, these are engineered to deliver drugs in a controlled manner, ei- ther at specific intervals or in reaction to external stimuli.[3–6] This method can be aligned with the human body's natural rhythms, such as circadian cycles.[7] It is particularly beneficial for con- ditions that require variable dosing[8] or precise timing of drug administration,[9] such as diabetes,[10] car- diovascular diseases,[11] and chronic pain management.[12] By synchronizing drug re- lease with biological needs, this method enhances therapeutic efficacy while mini- mizing

side effects, such as limiting sys- temic circulation and preventing off-target release, which reduces drug waste and po- tential toxicity.

The concept of on-demand drug release relies on creating a system capable of re- sponding to specific stimuli. External stim- uli such as light,[13] temperature,[14] pH changes,[15] and mechanical forces[16] can be utilized to control drug release. Light has emerged as a desirable stimulus due to its non-invasive nature, high precision, and ability to be modulated spatially and temporally.[17–22]

Near-infrared (NIR) light is particu- larly suited for biomedical applications due to its longer wavelength compared to visible light. This characteristic enables it to penetrate tis- sues up to several centimeters deep with minimal damage or scattering.[23,24] Additionally, NIR light's capacity to activate light- sensitive materials or produce localized heat makes it an effective tool for facilitating on-demand drug release.[25]

Integrating plasmonic nanoparticles into drug delivery system can further enhance its capabilities.[26–28] Plasmonic nanopar- ticles, such as gold nanostars (Au NSs), exhibit a unique phenomenon known as localized surface plasmon resonance (LSPR).[29,30] This optical property enables nanoparticles to absorb light and convert it into localized heat.[29] When irradiated with NIR light, Au NSs efficiently generate heat within a confined area, causing structural or chemical changes in the surround- ing matrix that lead to drug release.[30] This photothermal effect is particularly beneficial for achieving on-demand drug release in drug delivery systems. Furthermore, Au NSs can be tuned to absorb light within the NIR tissue window (700–900 nm), a wavelength range that minimizes tissue damage while maximiz- ing therapeutic efficiency.[31,32] As a result, Au NSs are highly promising for applications such as photothermal therapy (PTT) and stimuli-responsive drug release.

Advanced techniques for nanomaterials fabrication, includ- ing electrospinning and electrospraying, have enabled the development of sophisticated nanostructures for drug delivery applications.[33–42] Electrospinning, a straightforward method, is widely used to produce nanofibers with high surface area, porosity, and tunable mechanical properties.[35] By applying an electric field to a polymer solution, electrospinning generates continuous nanofibers, which can serve as carriers for drugs or other therapeutic agents.[43] One of the most significant advancements in electrospinning is the development of coaxial electrospinning, a method that enables the simultaneous pro- cessing of multiple polymer solutions to produce bicomponent nanofibers.[44–46] This technique is advantageous for developing systems with controlled drug release profiles, as one component can encapsulate the hydrophilic drug, while the other imparts mechanical strength, allowing the utilization of the distinct properties of both polymers and preventing rapid dissolution in aqueous media. Additionally, since both polymer solutions are immiscible, coaxial electrospinning eliminates the need for surfactants or emulsions, simplifying the fabrication process while maintaining the integrity of each polymer component. The electrospraying method, closely related to electrospinning, has also gained attention for its ability to deposit nanoparticles onto nanofiber surfaces.[47–50] By applying an electric field to a liquid dispensed through a metal needle, electrospraying generates fine droplets that can be sprayed onto a substrate. This method is useful for incorporating plasmonic nanoparticles onto the surface of electrospun fibers.[51,52] The combination of electrospinning and electrospraying provides a powerful method for fabricating multifunctional nanostructures that integrate the benefits of nanofibers with the

stimuli-responsive properties of plasmonic nanoparticles. This study presents the design and fabrication of an on-demand drug delivery system based on bi-polymer nanofibers decorated with plasmonic Au NSs. The system was fabricated using combination of coaxial electrospinning and electrospraying, resulting in nanofibers composed of a poly(3-hydroxybutyrate co-3-hydroxyvalerate) (PHBV, a polyhydroxyalkanoate-type polymer), and poly(lactide-co-glycolide) (PLGA) surface-decorated with Au NSs. PHBV, selected for its biodegradability and bio- compatibility, facilitates the incorporation of hydrophilic drugs. PLGA, a hydrophobic polymer, provides sustained drug re- lease by protecting the hydrophilic polymer from quick dissolving while maintaining structural integrity. The incorporation of Au NSs enables the platform's NIR responsiveness for precise photothermal-triggered drug release.

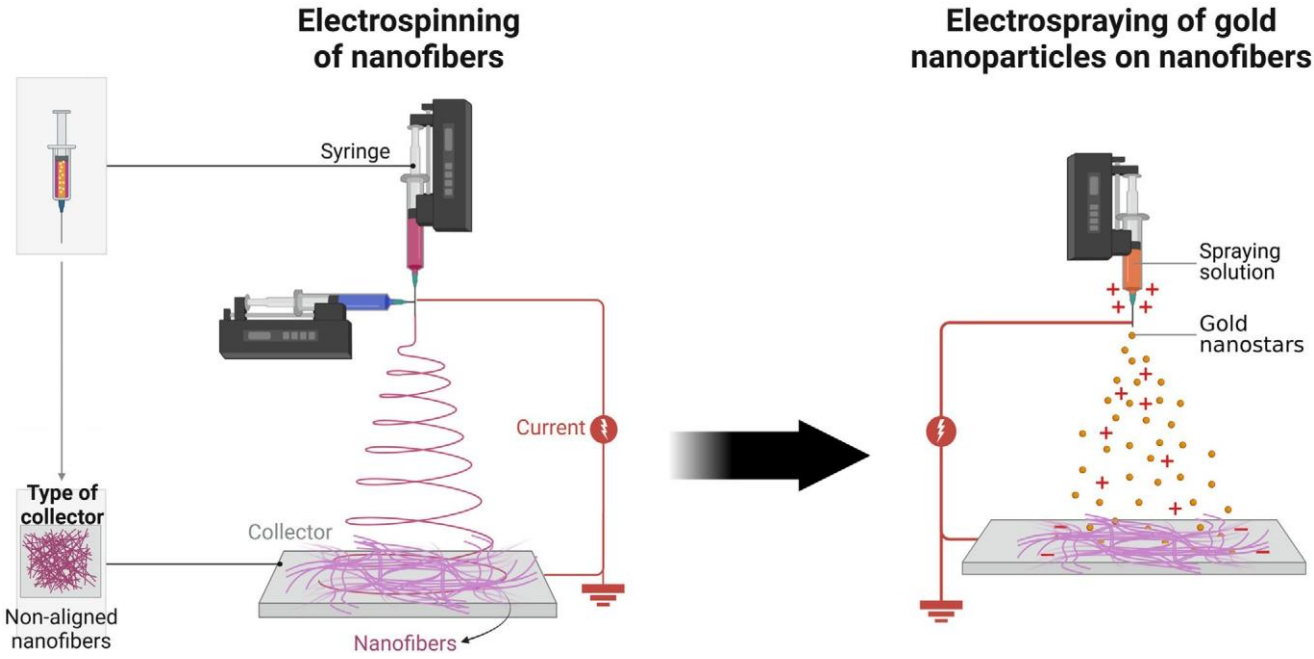

Figure 1. The scheme illustrating the fabrication process, where PHBV and PLGA are assembled in a coaxial electrospinning setup, followed by the Au NSs electrospraying on the structure.

2. Results and Discussion

2.1. Platform Architecture

The nanofibrous system incorporating PHBV, PLGA, and Au NSs was fabricated using a combined electrospinning and elec- trospraying method. The process involved coaxial electrospin- ning of PHBV and PLGA solutions to create nanofibers, with electrospraying of Au NSs dispersed in ethanol and DI water. The hydrophilic drug model was dissolved in the PHBV compo- nent of the fiber, while the PLGA component provided mechan- ical stability. The fibers were then decorated with gold nanopar- ticles. By integrating PHBV and PLGA, the fiber fabrication pro- cess facilitated the incorporation of RhB as a model drug and

enabled the decoration of the fiber surface with plasmonic Au NSs. The schematic of the electrospinning-electrospraying setup is depicted in Figure 1, highlighting the formation of the bicom- ponent fibers. This configuration provided a structure with dis- tinct advantages for drug delivery applications. Specifically, the plasmonic properties of Au NSs facilitated a thermally responsive drug release mechanism, with the Au NSs generating localized heat upon exposure to NIR light.[9,29,34] This photothermal effect of Au NSs offers a precise trigger for controlled drug release, en- hancing the system's potential for stimuli-responsive drug deliv- ery systems. The induced heat can accelerate the release kinetics of the encapsulated drug within the electrospun fibers, allowing for an on-demand release profile. This setup shows promise for applications requiring precise drug release modulation, leverag- ing both the biocompatibility of PHBV and PLGA, and the NIR- responsive capabilities of plasmonic nanoparticles in the fibers.

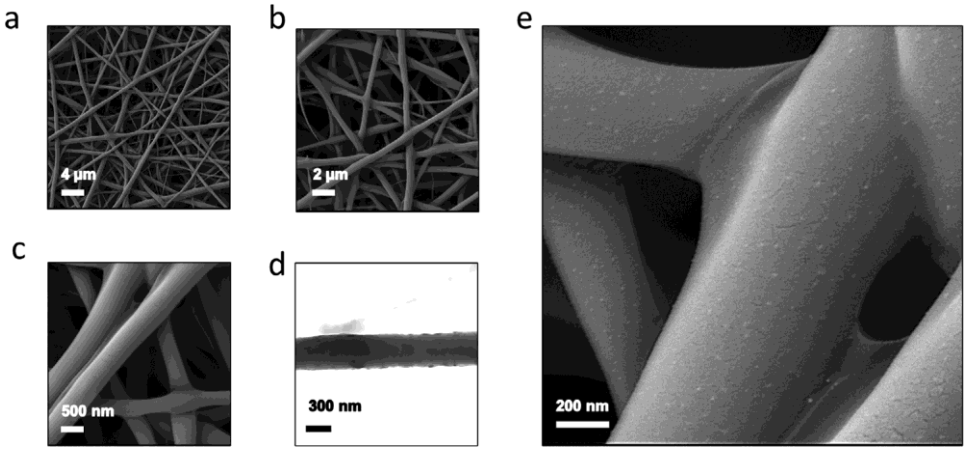

Figure 2. Morphology of the bi-polymer electrospun fibers. a) FE-SEM micrograph showing the nanofibrous platform structure, b) a detailed close-up view of the morphology, and c) an even more magnified view highlighting finer structural details. d) TEM micrograph illustrating the decorated with Au NSs. e) FE-SEM micrograph displaying the distribution of Au NSs on the platform surface.

2.2. Morphological Characterizations

Field emission scanning electrosn microscopy (FE-SEM) was uti- lized to to investigate the morphology of the nanofibers and the distribution of Au NSs on the fiber surfaces, verifying their successful integration. As shown in Figure 2a–c, the fibers ex- hibit a smooth, bead-free morphology, indicating the quality of the electrospinning process. Moreover, the morphology of the monolithic fibers of PLGA, and PHBV can be seen in Figure S1 (Supporting Information). Diameter distribution analysis con- firms that the nanofibers have a consistent average diameter of 702 ± 50 nm, a uniformity essential for reliable comparisons of drug release kinetics across different fiber types. Addition- ally, the transmission electron microscopy (TEM) micrographs in Figure 2d present a closer examination of a single coaxial PHBV-PLGA fiber, highlighting the distinct decoration with Au NSs. The TEM images show clear contrasts between the Au NSs and fiber matrix created by electron beam diffraction, which

un- derscores the distinct phase separation and confirms the suc- cessful integration and distribution of Au NSs on the fibers. Figure 2e provides a detailed view of the Au NSs distribution on a single fiber surface, revealing uniform dispersion across the fiber.

2.3. Physio-Chemical Characterizations

The attenuated total reflactance Fourier transorm infrared (ATR- FTIR) spectra of the nanofibers, shown in Figure 3a, reveal distinct peaks that help identify the fibers' chemical composi- tion and structural features. In the spectra of both PLGA and PHBV fibers, a prominent peak at 1750 cm−1 corresponds to the carbonyl (C═O) stretch, characteristic of both PLGA and PHBV. This peak indicates the carbonyl group in both poly- mers, confirming the presence of this functional group in the nanofibers. In addition, both PHBV and PLGA display C─O stretching bands at ≈1278 and 1054 cm−1, as well as C–H stretch- ing bands ≈2974 and 2935 cm−1, all of which are fingerprints of ester and methylene groups that are present in both ma- terials. Additionally, a peak at 1080 cm−1 is observed in the spectra of both PLGA and bicomponent fibers, corresponding to the C─O─C stretching vibration associated with ester link- ages in the polymer backbone. Furthermore, in Figure S2 (Sup- porting Information), the magnified ATR-FTIR results are pro- vided for better clarity and visibility of the relevant spectral fea- tures. This observation supports that both polymers formed a blend in the fibrous structure. Differential scanning calorime- try (DSC) was employed to characterize the thermal properties of the PHBV, PLGA, and PHBV-PLGA nanofibers, focusing on

their melting temperatures (Tm) and glass transition tempera- tures (Tg) to assess structural and compositional attributes. The resulting DSC thermograms, shown in Figure 3b, reveal dis- tinct thermal transitions for each fiber type. In the DSC ther- mogram of pure PHBV fibers, a sharp endothermic peak is ob- served at ≈168.2 °C, representing the Tm. This prominent peak suggests a well-defined crystalline structure typical of PHBV. The PLGA nanofibers exhibit a single Tg at 52.3 °C, charac- teristic of this polymer.[9] In contrast, the DSC thermogram of the bicomponent nanofibers, composed of PLGA and PHBV, ex- hibits a significantly shifted melting temperature. The PHBV- PLGA Tm is observed at 92.5 °C, a marked decrease, suggest- ing the PLGA presence influence in altering the bi-polymer sys- tem's thermal properties. The observation of a single Tg sug- gests thermodynamic miscibility between the PLGA and PHBV, indicating a blend with molecular compatibility at the poly- meric domains.[53] Thermal degradation of PLGA, PHBV, and PHBV-PLGA nanofibers was studied using thermogravimetric analysis (TGA), as shown in Figure 3c. The TGA curves reveal distinct thermal behavior based on the composition and molec- ular weight of the polymers.[47] The main mass loss occurred at different temperatures for each sample, as the molecular weight and composition of the polymer influenced the degradation tem- peratures. For pure PLGA fibers, the degradation initiated at ≈345 °C and completed at ≈450 °C, resulting in nearly 100% weight loss. This behavior is consistent with previously reported data for PLGA, which shows a primary decomposition tempera- ture near 400 °C.[54]

The DTG (first dericative) curves of PLGA and PHBV-PLGA (Figure 3d) show a peak at 385 °C, corresponding to the decom- position of the PLGA chains. In contrast, PHBV degradation occurs in a single-step process, with fibers exhibiting a lower decomposition temperature than PLGA, with degradation occur- ring between 250 and 300 °C. This suggests that PHBV degrades at a lower temperature due to its different molecular structure and weaker interchain

interactions compared to PLGA.[54,55] For the bicomponent fibers, the TGA curve exhibited a complex degradation profile with bimodal behavior. The first peak, ap- pearing at temperatures similar to PHBV degradation, suggests that the PHBV component decomposes first. The second peak, observed at higher temperatures, is related to the degradation of the PLGA segments within the PHBV-PLGA nanofibers. This two-stage degradation is indicative of the polymers forming a blend, where the different components degrade at different temperatures due to their distinct chemical and physical properties.

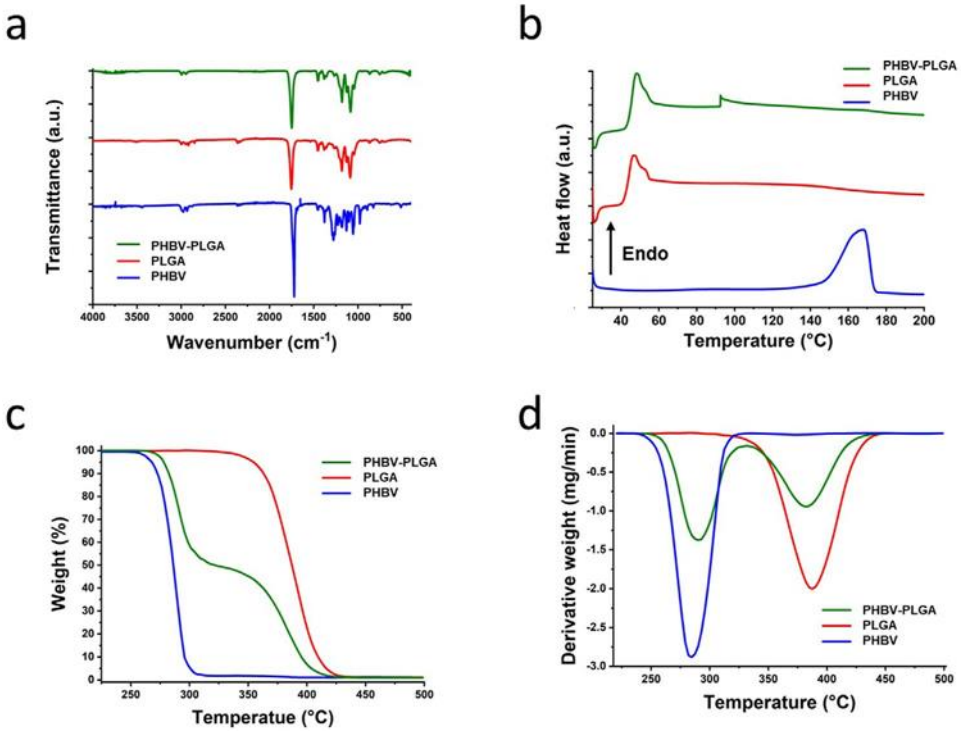

Figure 3. Chemical and thermogravimetric properties. a) ATR-FTIR spectra comparing PLGA and PHBV nanofibers with the PHBV-PLGA. b) DSC graph of the bicomponent fibers, demonstrating the presence of both PHBV and PLGA in the structure. c) TGA curves showing weight percentage versus temperature for monolithic fibers and the bi-polymer fibers, d) DTG graphs of PHBV and PLGA monolithic fibers, alongside the results for PHBV-PLGA electrospun fibers providing insights into their thermal stability and degradation profiles.

2.4. Cell Studies

To assess the biological properties of the proposed fibrous ma- trices and their potential for biomedical applications, the interaction of these materials with L929 fibroblast cells was inves- tigated. The study evaluated the impact of bicomponent fibers on the viability of cells. No significant differences were observed between the conditions at the day 1-time point, indicating that the cells attached to the placed surface in the same manner for all groups. However, starting from day 3, significant differ- ences were noted between the samples and the control (CTRL)

on each analyzed day (Figure 4). Despite these differences, the cells continue to show a preference for proliferation, which indi- cates that the developed materials are fully biocompatible. When comparing the PLGA and PHBV-PLGA groups, it was observed that the PLGA is more biocompatible. It is similar to the previous experiment,[9] where PLGA showed slightly higher cell viability compared to the bi-polymer sample. The lower biocom- patibility of the PHBV-PLGA system compared to PLGA alone may be due to combined differences in surface properties, degra- dation, mechanical properties, and molecular interactions.[56] Small visible differences in cell adhesion were noticeable on the first day after seeding, and this hydrophilicity likely af- fected cell proliferation on subsequent days. Moreover, differ- ences in material chemistry may affect interactions with extra- cellular matrix proteins, affecting cell adhesion, migration, and proliferation.

SEM images captured after 3 and 7 days of seeding clearly demonstrated cell attachment on day 3, with cell protrusions adhering to the substrate (Figure 5). By day 7, the cells exhibited a spindle shape, indicating spreading and proliferation on the sample surface with no evident differences in cell morphology among the tested conditions. These results demonstrated the biocompatibility of the fibrous structures, highlighting their suitability for cell attachment, survival, spreading, and proliferation. To further support this, confocal images of Phalloidin/DAPI stained samples were analyzed, revealing the cell cytoskeleton and nuclei after 3 and 7 days of culture. Initially, L929 fibroblasts appeared rounded, but over time, they began to adopt a typ- ical spindle shape. This was followed by cell proliferation and the eventual coverage of the entire matrix surface. In the case of PHBV-PLGA fibers, which had the lowest cell count, individ- ual cells adhered to the surface with more space around them, resulting in a more elongated shape of actin fibers. This is due to cellular interactions aiming to connect with each other to cre- ate an extracellular matrix. In contrast, cells seeded on PLGA and CTRL samples were more crowded and covered the entire surface (Figure 6).

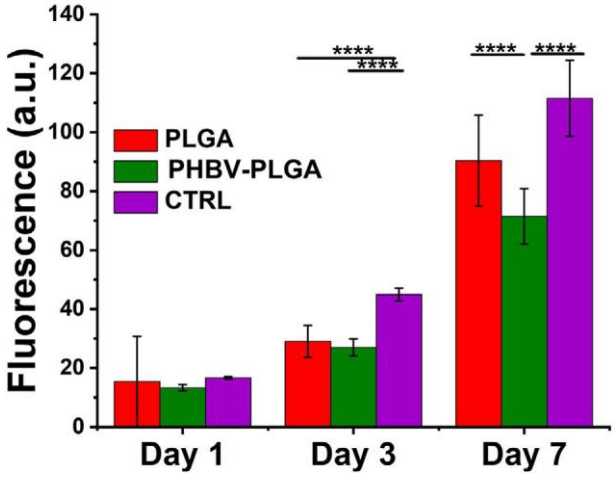

Figure 4. Viability of L929 fibroblast cells seeded on PLGA, PHBV-PLGA fibrous structures, and CTRL up to 7 days of culture.

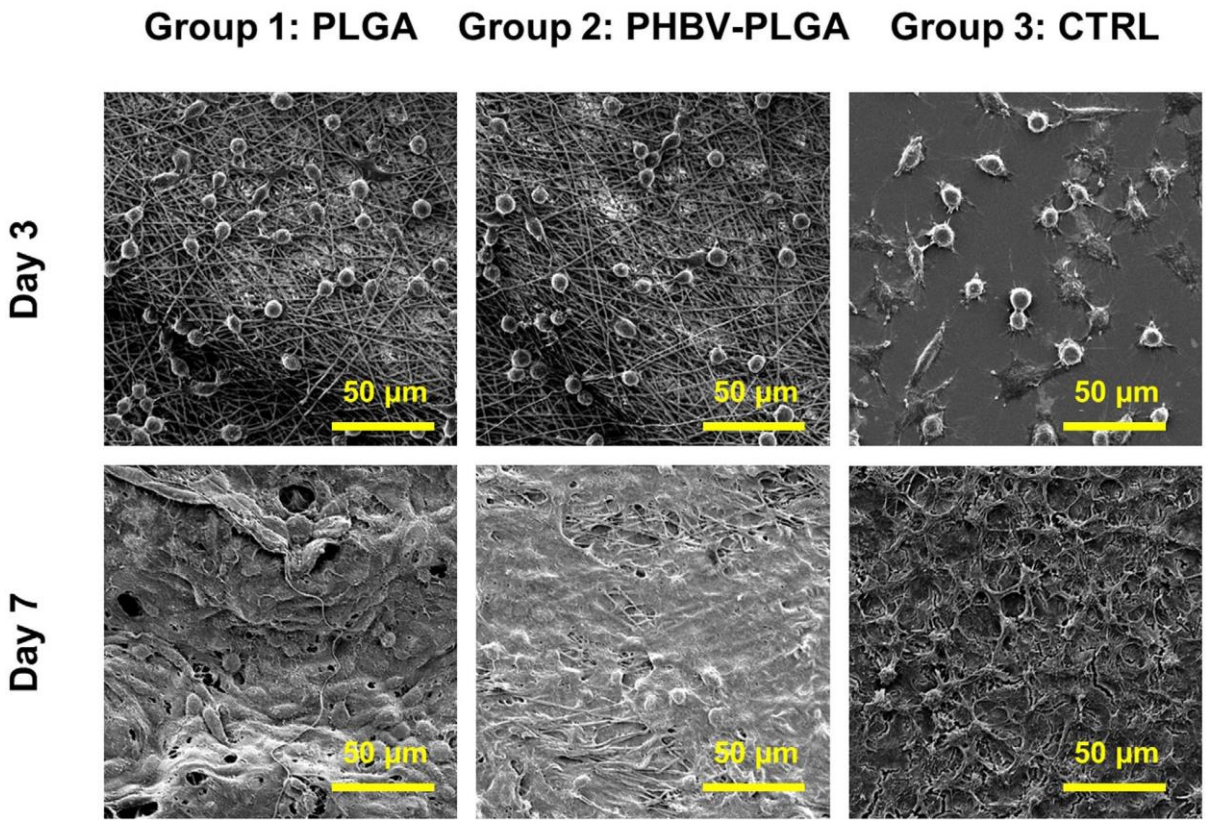

Figure 5. SEM images of L929 fibroblasts cultured PLGA, PHBV-PLGA fibrous structures, and CTRL for 3 and 7 days. Scale bar: 50 µm.

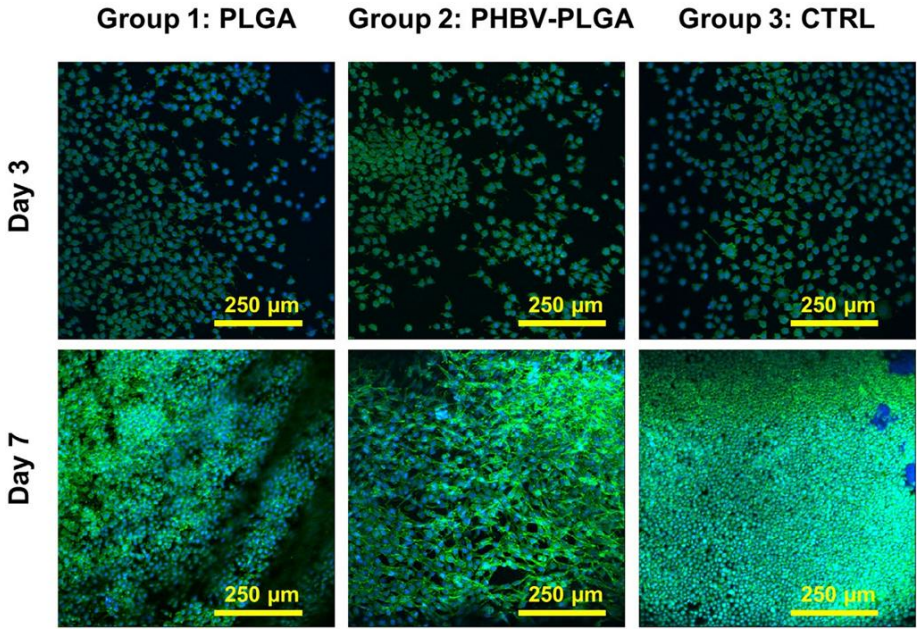

Figure 6. Confocal images of cells seeded on PLGA, PHBV-PLGA, and CTRL and stained with Phalloidin (green color) for cell cytoskeleton visualization and DAPI (blue color) for individuating the cell nuclei. Scale bar: 250 µm.

2.5 Thermal-Response Characterizations

The nanofibrous system was functionalized with Au NSs on its surface and loaded with RhB, enabling an efficient photothermal response under NIR light. The incorporation of plasmonic Au NSs endowed the fibers with a strong NIR light absorption capacity, converting absorbed light into localized heat due to the high photo-response efficiency of the particles. The NIR responsiveness of the system was assessed using a thermal camera, with irradiation provided by an 808 nm wavelength NIR laser at a power density of 2.5 W cm^{-2}. This laser power was selected from powers from 500 to 3000 mW to trigger drug release from the platform to achieve the targeted temperature. The relationship between laser power and temperature is shown in Figure S1 (Supporting Information). During irradiation, thermographic images captured the progressive heating of the system, allowing for a precise assessment of the photothermal effect.

A crucial consideration for the system's efficiency in drug delivery was the placement of Au NSs on the fiber surface rather than within the structure. The bicomponent nanofibers, decorated with Au NSs, demonstrated significant NIR light absorption, converting this energy into heat. The thermographic images, illustrated in Figure 7, highlight the platform's temperature increase in both dry and wet states under NIR exposure. Initial tests in the dry state provided insight into the maximum heat generation potential of the bi-polymer structure. Subsequent tests in an aqueous environment demonstrated the platform's utility in drug delivery applications, where heating the surrounding medium is crucial for effective release modulation. Upon NIR irradiation, the dry fibers reached a peak temperature of 79.9 °C while the fibers in water achieved a temperature of 48.6 °C (Figure 7a,c), confirming the system's efficacy in reaching pwdtargeted temperatures for both wet and dry platforms to trigger drug release and perform PTT. Figure S4 (Supporting Information) demonstrate the NIR response of the control samples with- out Au NSs. As the results show, the laser was unable to increase the temperature of the dry sample by more than 5 °C, and for the wet sample, the temperature increase was <3 °C. This further highlights the contribution of the gold nanostars to the observed photo-response and temperature rise.

The study investigated photothermal response under cyclic ir- radiation to further explore the potential application of these elec- trospun mats. This approach assessed the system's stability, resilience, and sustained photothermal efficacy, which are essen- tial for drug delivery applications. Cyclic irradiation mimicked real-world conditions of intermittent light exposure, providing insights into the durability of the photothermal properties under repeated use. Results indicated that for both dry and wet sam- ples, the surface temperature of the electrospun mats increased rapidly within the first 15 sec of NIR irradiation, stabilizing at ≈80 °C for dry samples and 48 °C for wet samples (as shown in Figure 7b,d). The stability to achieve the same temperatures simultaneously across all irradiation cycles supports the platform's potential as an effective on-demand drug carrier, demonstrating its capability to maintain consistent temperatures conducive to controlled drug release and therapeutic applications.

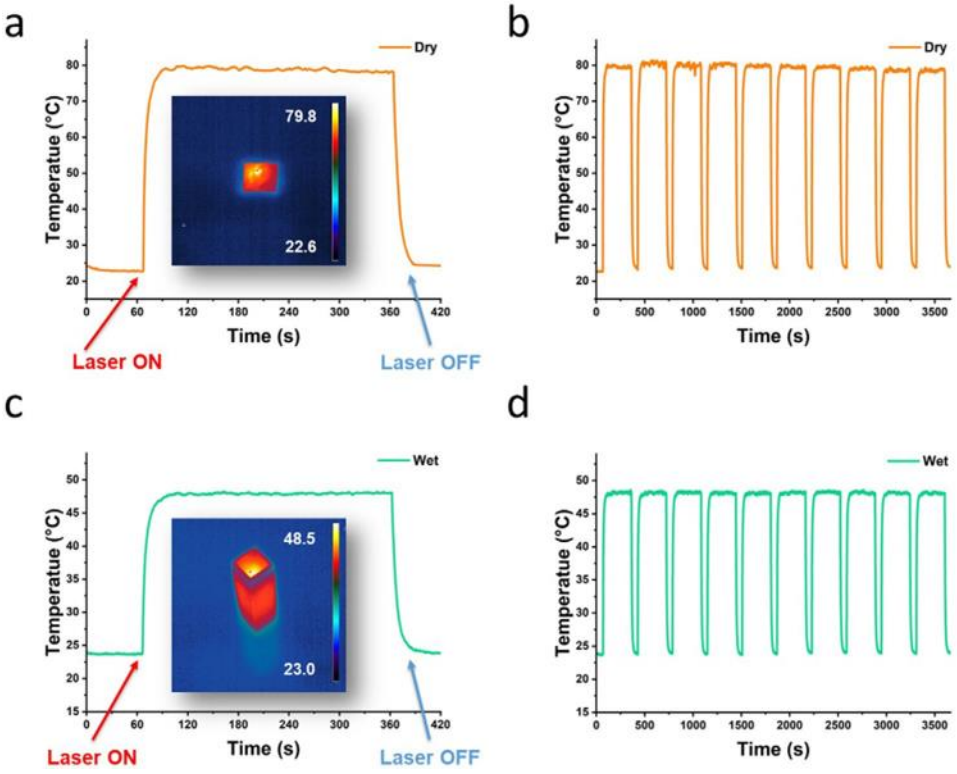

Figure 7. Photo-responses of the platform. a) IR thermogram images of the dry nanofibers, captured during 5 min of irradiation, with a thermographic image inset of the irradiated sample. b) Rapid increase in surface temperature of the dry nanofibrous mats during 10 cycles of NIR irradiation. c) Temporal plots depicting the platform's behavior under NIR irradiation for wet samples, with an inset of mats, maintaining 48.5 °C. d) Cyclic increase in the temperature of the electrospun mats during 10 cycles of NIR irradiation for wet samples.

2.6. Drug Release Studies

The release behavior of RhB across various platforms is illus- trated in Figure 8, including monolithic PHBV, PLGA, and bicomponent fibers. Moreover, the bipolymer platform is further divided into NIR irradiation and non-irradiated conditions. The irradiation process involved utilizing a laser to heat the plat- form locally (Figure 8a), significantly impacting the drug release profile. Upon NIR irradiation, the temperature of the platform rose, causing an enhanced release of RhB compared to non- irradiated samples. The cumulative release of RhB over 14 days (Figure 8b) highlights the controlled release characteristics of RhB from PHBV, PLGA, and PHBV-PLGA fibers, with the bipolymer fibers exhibiting a regulated release profile. Figure 8c depicts the light-triggered release from bicomponent fibers dec- orated with Au NSs under cyclic irradiation conditions. Each cy- cle consisted of 5 min of laser exposure. The periodic release be- havior demonstrates the potential for on-demand drug delivery, as the NIR light acts as a stimulus to accelerate drug release. Notably, incorporating Au NSs enabled the platform to act as a local- ized heat source, enhancing drug release. Figure 8d provides fur- ther insights into the hourly release rate for irradiated and non- irradiated samples. The irradiated fibers exhibited a significantly higher initial release, particularly within the first few hours of the experiment, achieving approximately twofold increase in re- lease than the non- irradiated control. This highlights the capability of the Au NSs-integrated system to achieve a

rapid and efficient drug release upon demand. Additionally, the mechanism of RhB release is attributed to desorption from the nanofibers, followed by diffusion through the platform's porous structure. Laser-induced temperature increases accelerate these processes, making this platform an ideal candidate for modulated drug release applications. These findings underscore the potential of the bicomponent system for long-term, controlled, and stimuli- responsive drug delivery.

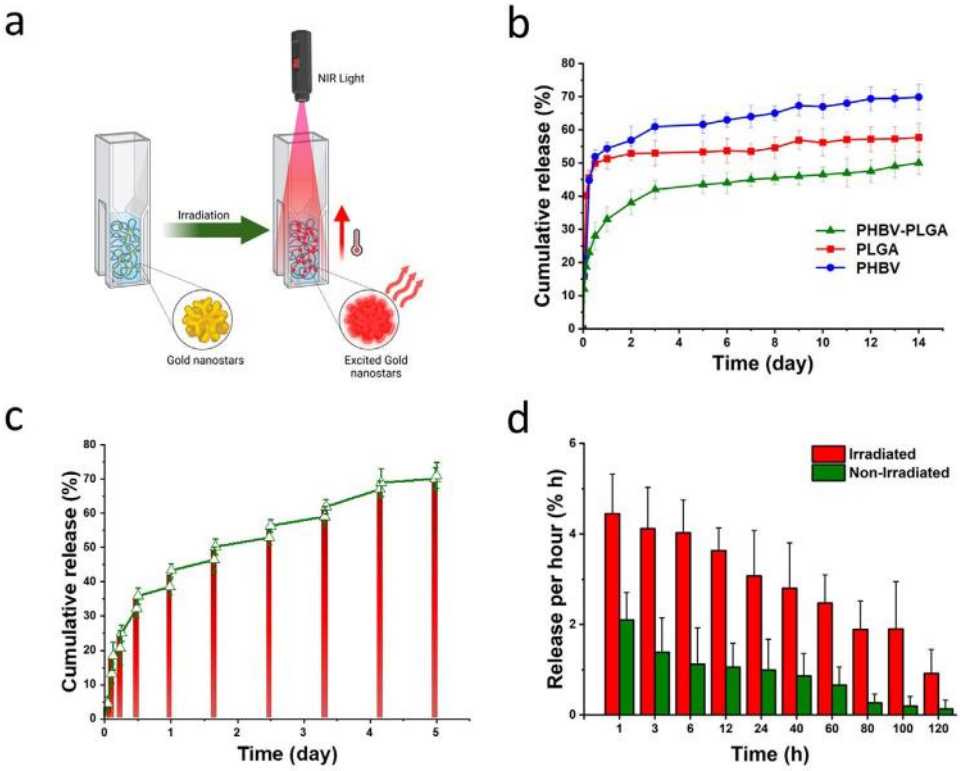

Figure 8. Drug release properties of the prepared platforms: a) The scheme illustrates the platform's temperature increase under NIR irradiation, which facilitates the enhanced release of RhB. b) Cumulative RhB release from three samples: monolithic PLGA, PHBV, and non-irradiated bi-polymer fibers. c) Cumulative RhB release after 10 cycles of NIR light irradiation, with red vertical lines marking each irradiation cycle. d) The bar chart shows the RhB release rate per hour from non-irradiated and irradiated bicomponent fibers, highlighting the release kinetics at different time intervals. The irradiated sample bar graph shows the laser-triggered release of RhB and emphasizes the fabricated platform's photo-responsive behavior.

3. Conclusion

This study demonstrates the successful development of a photo- responsive nanofibrous platform. The platform comprises PLGA and PHBV electrospun fibers decorated with Au NSs, designed explicitly for on-demand drug delivery. In contrast to monolithic fibers, this system exhibits a more controlled and sustained drug release profile, with enhanced release rates under NIR light stim- ulation. The drug delivery system achieves 50% release efficiency without laser triggering after 5 days. However, this efficiency in- creases to 70% over the same period when the system is stimu- lated with the NIR laser. While the monolithic fibers showed a typical

burst release limiting their potential for sustained thera- peutic delivery, this platform enabled gradual release triggered by NIR-induced heating of Au NSs. The platform's ability to undergo repeated cycles of drug release further emphasizes its robustness and suitability for dynamic, on-demand therapeutic applications.

4. Experimental Section

Materials: Poly(3-hydroxybutyrate-co-3-hydroxyvalerate) (PHBV, Mw = 570–590 kDa, 80181-31-3, Sigma Aldrich), poly(lactide-co-glycolide) (PLGA, Mw = 600–620 kDa, 26780-50-7, Evonik), 2,2,2-trifluoroethanol (TFE, 99.0%, Sigma–Aldrich), 2-propanol (99.5%, Sigma–Aldrich), 1,1,1,3,3,3-hexafluoro-2-propanol (HFIP, 99.0%, Sigma–Aldrich), ethanol (96.0%, Sigma–Aldrich), glutaraldehyde (50.0%, Sigma–Aldrich), paraformaldehyde (95.0%, Sigma–Aldrich), Rhodamine B (RhB, 95.0%, Sigma–Aldrich), gold nanostars (Au NSs, λ = 800 nm, OD = 1, C = 0.04 mg mL−1, nanoComposix), phosphate buffer saline (PBS, Sigma–Aldrich), Dulbecco's modified Eagle's medium (DMEM, Gibco Invitrogen), L929 murine fibroblast cells (Sigma–Aldrich), fetal bovine serum (FBS, Gibco Invitrogen), penicillin-streptomycin (PS, Gibco Invitrogen), Alexa Fluor 488 Phalloidin (Thermo-Fisher Scientific), EDTA-trypsin (Gibco Invitrogen), PrestoBlue reagent (Thermo-Fisher Scientific), hexamethyldisilazane (HMDS, Sigma–Aldrich), Triton X-100 (Sigma–Aldrich), bovine serum albumin (BSA, Sigma–Aldrich), and DAPI (Sigma–Aldrich).

Platform Preparation: The electrospun fibers were prepared using a coaxial electrospinning process. The PHBV precursor solution was a 2.0% (w/v) in TFE, while the PLGA precursor solution was a 5.0% (w/v) dis- solved in HFIP.

To prepare the solution for electrospraying Au NSs, 45 µL of gold nanostars at a concentration of 1 OD were mixed with 55 µL of an equal ratio (1:1) of ethanol and deionized (DI) water. The coaxial electrospinning setup consisted of a 21G needle for the inner needle and a 16G needle for the sheath needle at a distance of 20 cm from a grounded flat collector. The applied voltage to both needles was 15 kV. Flow rates were optimized at 300 µL h^{-1} for the PHBV solution and 550 µL h^{-1} for the PLGA solution. Electrospinning was conducted in a chamber at 24 °C and 48% relative humidity. Three milligrams of RhB was magnetically stirred with 5 mL of the PHBV solution in TFE to prepare drug-loaded fibers. Homopolymer nanofibers of PHBV and PLGA were also fabricated as controls. These control fibers were designed with the same concentration of RhB as the bicomponent fibers. PHBV and PLGA fibers were electrospun using a 26G needle, with a voltage of 15 kV and a flow rate of 600 µL h^{-1}, at a 20 cm distance from the flat collector. The electrospraying technique was used to spray the Au NSs on the surface of the nanofibers. The mentioned solution of Au NSs in deionized water and ethanol was loaded into a 1 mL syringe fitted with a 26G needle. The electrospraying was performed at 15 kV, with a flow rate of 600 µL h^{-1}, and using the same collection parameters as the electrospinning process.

Morphological Characterizations: A detailed analysis was performed using FE-SEM and TEM to investigate the morphological structure of the fabricated nanofibrous materials. Before imaging, the samples were coated with a 5 nm gold layer using a DII-29030SCTR JEOL Smart Coater.

This preparation step was crucial for achieving clear and precise micro- scopic results. The analysis was conducted with a ZEISS Crossbeam 350 FIB-SEM microscope, operating at an accelerating voltage of 5 kV and a working distance of 5.5 mm for FE-SEM and 2.0 mm for TEM.

Chemical Characterizations: The chemical composition of the materi- als was analyzed using a ATR-FTIR spectroscopy. ATR-FTIR spectroscopy was used to examine the functional groups present in the materials. Mea- surements were performed with a Bruker Vertex70 FTIR spectrometer, which measured transmittance across a wavenumber range of 4000–400 cm^{-1}, at a resolution of 2 cm^{-1} for precise spectral data. To ensure accuracy and reproducibility, each sample underwent eight scans. The Bruker Vertex70 Spectrometer was equipped with a diamond crystal as its ATR element.

Thermal Characterizations: TGA was performed using a TA Instruments Q600 thermogravimetric analyzer by heating from 30 to 500 °C with a ramp of 10 °C min^{-1} in air. DSC analyses were conducted using a TA Instruments Q2000 DSC by varying the temperature from 20 to 200 °C with a heating ramp of 5 °C min^{-1} in nitrogen.

In Vitro Cell Studies: Culture of L929 Fibroblast Cells: L929 murine fibroblast cells were cultured in DMEM supplemented with 10% (v/v) FBS and 1% (v/v) PS in an incubator at 37 °C with 5% CO_2. The culture medium was refreshed every two days. Cell passaging was performed when the cell confluence reached ≈80%. For seeding, cells were detached by adding 0.05% EDTA-trypsin for 3 min and incubating the cells at 37 °C with 5% CO_2. Subsequently, cells were collected in a Falcon tube and centrifuged at 1200 rpm for 5 min. After centrifugation, a pellet of cells was visible at the bottom of the tube. Cells were then resuspended in 1 mL of culture medium and counted. Finally, the cell suspension was further diluted in a culture medium to achieve a convenient cell density for seeding the samples.

Sample Sterilization and Seeding: Two groups of fibrous samples (PLGA fibers, and PHBV-PLGA fibers) were electrospun onto coverslips (diameter = 1.5 cm) and sterilized by exposure to ultraviolet (UV) light (30-min cycle for each side). Samples were placed in 24-well plates, and L929 fibroblast cells were seeded on top of the fibrous samples at a density of 104 cells cm−2.[57] The control condition was also tested by seeding tissue culture plates (CTRL) at the same cell density. All samples were cultured for up to 7 days.

Cell Viability: The viability of the cells was measured using the Presto- Blue assay. Fibrous samples and CTRL seeded with L929 fibroblasts were treated with a solution of 10% (v/v) PrestoBlue reagent in a culture medium and incubated for 2 h at 37 °C with 5% CO_2. Five replicates of each sample were analyzed at three selected time points: 1, 3, and 7 days after cell seeding. After 2 h of incubation, 100 µL aliquots of the PrestoBlue solution were transferred to a 96-well plate and analyzed at an excitation wavelength of 530 nm and an emission wavelength of 620 nm using a fluorometer plate reader (Fluoroskan Ascent Microplate Fluorometer, Thermo Scientific).

Cell Morphology: The morphology of L929 fibroblasts in contact with fibrous samples and tissue culture plates was evaluated by means of scanning electron microscopy (SEM) and confocal microscopy.

For SEM imaging, the samples were initially fixed in 3% ice-cold glutaraldehyde for 3 h. Subsequently, the samples were washed three times in DI water and dehydrated by immersing

them in solutions with increas- ing ethanol concentrations (50%, 70%, 90%, and 100%) for 15 min each. Hexamethyldisilazane was then introduced to the constructs, and the samples were air-dried overnight under a fume hood. The samples were then sputter-coated with a thin layer of gold before being analyzed using a SEM. For the confocal visualization, the cell cytoskeleton and nuclei were stained by fixing the samples in 4% (v/v) paraformaldehyde for 15 min at room temperature. The samples were then washed three times in PBS and treated with a solution of 0.1% (v/v) Triton X-100 for 15 min. After washing, a solution of 1% (w/v) BSA with 0.1% (v/v) Triton X-100 for 1 h. Then, the samples were washed and incubated with 1% BSA with 0.1% Triton X-100 + solution of 1:40 Alexa Fluor 488 Phalloidin for 1 h in the dark. Finally, the nuclei were stained by adding a 1:500 DAPI solution in PBS for 10 min. Samples were washed three times, and cell cytoskeleton and nuclei were visualized using a confocal microscope (Leica). Staining was performed on three replicates per condition at 3 and 7 days after cell seeding.

Photothermal-Response Characterizations: Thermo-optical experiments were conducted to study the thermal response of Au NSs-decorated bicomponent nanofibers using a Laser MDL-H-808 from CNI. This NIR laser was configured to operate at a wavelength of 808 nm, with adjustable power settings ranging from 500 to 3000 mW. This laser was selected due to its overlap with the gold nanostar's maximum absorbance wavelength. The experiments captured temporal and spatial thermal behavior using a high-resolution FLIR A655sc thermal camera, at 640 × 480 pixels resolution and a temperature accuracy of 0.2 °C. The FLIR camera was integrated with FLIR Research Studio software. The experiments included cyclic thermal analysis, where the samples were exposed to 5 min of irradiation followed by a 1-min cooling period, repeated over ten cycles.

Drug-Release Analysis: The release behavior of RhB from PHBV, PLGA, and PHBV-PLGA electrospun fibers was studied at 37 °C. The electrospun mats, 2 cm in diameter and containing ≈50 μg of RhB, were immersed in 1 mL of PBS solution in a vial. Each vial was sealed and wrapped in aluminum foil to prevent evaporation and light exposure. At set intervals (1, 3, 6, 12, and 24 h), the supernatant solution was replaced with fresh PBS maintained at 37 °C. Temperature monitoring was performed using an FLIR thermal camera. For the next 3 days, RhB release was measured every day, followed by daily measurements over the subsequent 10 days. The fluorescence intensity of released RhB was determined using a Fluoroskan Ascent TM Microplate Fluorometer (Thermo Scientific) with an excitation-emission range of 530–620 nm. The fluorescence data were analyzed against a calibration curve to calculate RhB concentrations. Release experiments involved irradiation with an 808 nm diode laser (MDL-H- 808) for gold nanostars-decorated systems. Decorated bicomponent fiber mats, 2 cm in diameter, were suspended in 1 mL of deionized water in sealed vials secured with parafilm. Samples underwent cyclic irradiation, with 5 min of NIR laser exposure and 55 min of rest. After each sequence, the supernatant was collected and analyzed using the fluorometer to quantify the RhB released.

Statistical Analysis: The data are shown as mean values ± standard deviation (SD). Statistical analysis was performed using a one-way ANOVA test. Each drug release experiment was conducted in three replicates for each platform to ensure the reliability and reproducibility of the results.

Supporting Information

Supporting Information is available from the Wiley Online Library or from the author.

Acknowledgements

This work was supported by the National Science Centre (NCN) SONATA BIS Project No. 2020/38/E/ST5/00456 and the Polish National Agency for Academic Exchange (NAWA) under Bekker NAWA Programme, grant number: BPN/BEK/2021/1/00161. The Authors are grateful for the sup- port provided by the National Agency for Academic Exchange (NAWA) grant no. PPI/APM/2018/1/00045/U/001. Figures 1 and 8 were partially created with Biorender. P.N. and F.P. acknowledge the financial support from the Polish Ministry of Science and Higher Education through schol- arships for outstanding young scientists.

Conflict of Interest

The authors declare no conflict of interest.

Data Availability Statement

The data that support the findings of this study are available from the cor- responding author upon reasonable request.

Keywords

electrospun nanofibers, NIR-light activation, on-demand drug delivery, plasmonic nanoparticles

References

[1] S. Campbell, N. P. Rivera, S. Said, A. Lam, L. Weir, J. Gour, N. M. B. Smeets, T. Hoare, ACS Appl. Mater. Interfaces 2023, 15, 48892.

[2] S. Ciancia, A. Cafarelli, A. Zahoranova, A. Menciassi, L. Ricotti, Front. Bioeng. Biotechnol. 2020, 8, 519348.

[3] J. Gao, J. M. Karp, R. Langer, N. Joshi, Chem. Mater. 2023, 35, 359.

[4] D. Jain, R. Raturi, V. Jain, P. Bansal, R. Singh, Biomatter 2011, 1, 57.

[5] J. Liu, C. Detrembleur, B. Grignard, M. C. De Pauw-Gillet, S. Mornet,

M. Treguer-Delapierre, Y. Petit, C. Jérôme, E. Duguet, Chem. Asian J.

2014, 9, 275.

[6] J. S. Baek, C. C. Choo, C. Qian, N. S. Tan, Z. Shen, S. C. J. Loo, Small

2016, 12, 3712.

[7] A. Rajput, P. Pingale, D. Telange, S. Musale, S. Chalikwar, Heliyon

2024, 10, 29064.

[8] A. Geraili, M. Xing, K. Mequanint, VIEW 2021, 2, 20200126.

[9] M. A. Haghighat Bayan, Y. J. Dias, C. Rinoldi, P. Nakielski, D. Rybak,

Y. B. Truong, A. L. Yarin, F. Pierini, J. Polym. Sci. 2023, 61, 521.

[10] A. Kikuchi, T. Okano, Adv. Drug Delivery Rev. 2002, 54, 53.

[11] S. Jain, M. Malinowski, P. Chopra, V. Varshney, T. R. Deer, Expert Opin. Drug Delivery 2019, 16, 815.

[12] A. Maroni, L. Zema, M. Cerea, M. E. Sangalli, Expert Opin. Drug De- livery 2005, 2, 855.

[13] W. Zhang, T. Ji, Y. Li, Y. Zheng, M. Mehta, C. Zhao, A. Liu, D. S. Kohane,

Nat. Commun. 2020, 11, 1.

[14] S. W. Choi, Y. Zhang, Y. Xia, Angew. Chem., Int. Ed. 2010, 49, 7904.

[15] P. Gupta, K. Vermani, S. Garg, Drug Discov Today 2002, 7, 569.

[16] Y. Zhang, J. Yu, H. N. Bomba, Y. Zhu, Z. Gu, Chem. Rev. 2016, 116, 12536.

[17] M. Mathiyazhakan, Y. Yang, Y. Liu, C. Zhu, Q. Liu, C. D. Ohl, K. C. Tam, Y. Gao, C. Xu, Colloids Surf. B Biointerfaces 2015, 126, 569.

[18] C. J. Carling, M. L. Viger, V. A. Nguyen Huu, A. V. Garcia, A. Almutairi, Chem. Sci. 2014, 6, 335.

[19] C. S. Linsley, B. M. Wu, Ther. Delivery 2017, 8, 89.

[20] R. T. Zaman, A. Gopal, K. Starr, X. Zhang, S. Thomsen, J. W. Tunnell,

A. J. Welch, H. G. Rylander, Lasers Surg. Med. 2012, 44, 30.

[21] H. Hou, A. Nieto, A. Belghith, K. Nan, Y. Li, W. R. Freeman, M. J. Sailor, L. Cheng, Acta Biomater. 2015, 24, 309.

[22] S. Ferber, H. Baabur-Cohen, R. Blau, Y. Epshtein, E. Kisin-Finfer, O. Redy, D. Shabat, R. Satchi-Fainaro, Cancer Lett. 2014, 352, 81.

[23] D. J. Lim, H. Park, J. Biomater. Sci. Polym. Ed. 2018, 29, 750.

[24] Y. Yang, J. Aw, B. Xing, Nanoscale 2017, 9, 3698.

[25] A. Zhang, K. Jung, A. Li, J. Liu, C. Boyer, Prog. Polym. Sci. 2019, 99, 101164.

[26] C. J. Trout, J. A. Clapp, J. C. Griepenburg, New J. Chem. 2021, 45, 15131.

[27] H. Erdogan, M. Yilmaz, E. Babur, M. Duman, H. M. Aydin, G. Demirel, Biomacromolecules 2016, 17, 1788.

[28] N. M. Ngo, H. V. Tran, T. R. Lee, ACS Appl. Nano Mater. 2022, 5, 14051.

[29] M. A. Haghighat Bayan, C. Rinoldi, D. Rybak, S. S. Zargarian, A. Zakrzewska, O. Cegielska, K. Põhako-Palu, S. Zhang, A. Stobnicka- Kupiec, R. L. Górny, P. Nakielski, K. Kogermann, L. De Sio, B. Ding, F. Pierini, Biomater. Sci. 2024, 12, 949.

[30] B. J. Delgado-Corrales, V. Chopra, G. Chauhan, J. Mater. Chem. B, 2024, 13, 399.

[31] Y. Hang, A. Wang, N. Wu, Chem. Soc. Rev. 2024, 53, 2932.

[32] M. A. Haghighat Bayan, F. Afshar Taromi, M. Lanzi, F. Pierini, Sci. Rep.

2021, 11, 21144.

[33] A. Zakrzewska, M. A. Haghighat Bayan, P. Nakielski, F. Petronella, L. De Sio, F. Pierini, ACS Appl. Mater. Interfaces 2022, 14, 46123.

[34] M. A. Haghighat Bayan, C. Rinoldi, A. Kosik-Kozioł, M. Bartolewska,

D. Rybak, S. S. Zargarian, S. A. Shah, Z. J. Krysiak, S. Zhang, M. Lanzi,

P. Nakielski, B. Ding, F. Pierini, Adv. Mater. Technol. 2024, 10, 2400450.

[35] M. Bartolewska, A. Kosik-Kozioł, Z. Korwek, Z. Krysiak, D. Montroni, M. Mazur, G. Falini, F. Pierini, Adv. Healthc. Mater. 2024, 14, 2402431.

[36] A. Zakrzewska, S. S. Zargarian, C. Rinoldi, A. Gradys, D. Jarząbek, M. Zanoni, C. Gualandi, M. Lanzi, F. Pierini, ACS Mater. Au, 2023, 3, 464.

[37] M. Panahi-Sarmad, E. Chehrazi, M. Noroozi, M. Raef, M. Razzaghi- Kashani, M. A. Haghighat Baian, ACS Appl. Electron Mater. 2019, 1, 198.

[38] D. Rybak, C. Rinoldi, P. Nakielski, J. Du, M. A. Haghighat Bayan, S. S. Zargarian, M. Pruchniewski, X. Li, B. Strojny-Cie´slak, B. Ding, F. Pierini, J. Mater. Chem. B 2024, 12, 1905.

[39] P. Nakielski, D. Rybak, K. Jezierska-Wo´zniak, C. Rinoldi, E. Sinderewicz, J. Staszkiewicz-Chodor, M. A. Haghighat Bayan, W. Czelejewska, O. Urbanek, A. Kosik-Kozioł, M. Barczewska, M. Skomorowski, P. Holak, S. Lipin´ski, W. Maksymowicz, F. Pierini, ACS Appl. Mater. Interfaces 2023, 15, 58103.

[40] S. Abid, T. Hussain, Z. A. Raza, A. Nazir, Mater. Sci. Eng., C 2019, 97, 966.

[41] S. A. Shah, M. Sohail, P. Nakielski, C. Rinoldi, S. S. Zargarian, A. Kosik-Kozioł, Y. Ziai, M. A. H. Bayan, A. Zakrzewska, D. Rybak, M. Bartolewska, F. Pierini, Biomacromolecules 2024, 1, 140.

[42] S. S. Zargarian, B. Kupikowska-Stobba, A. Kosik-Kozioł, M. Bartolewska, A. Zakrzewska, D. Rybak, K. Bochenek, M. Osial,

F. Pierini, Mater. Today Chem. 2024, 41, 102281.

[43] K. Pirzadeh, L. Torkian, M. D. Asli, Mater. Today Commun. 2024, 41, 110439.

[44] D. F. Plascencia Martinez, J. M. Quiroz Castillo, A. Ospina Orejarena,

A. Pérez Gallardo, E. Méndez Merino, G. A. Trimmer López, I. Y. López Peña, D. Hernández Martínez, K. A. López Gastelum, A. A. Leyva Verduzco, A. S. Ledezma, M. M. Castillo Ortega, ACS Omega 2024, 9, 41157.

[45] J. Khan, A. Khan, M. Q. Khan, H. Khan, Next Mater. 2024, 3, 100138.

[46] P. R. Patel, D. Haemmerich, Polym. Adv. Technol. 2024, 35, e6507.

[47] A. R. Peringath, M. A. H. Bayan, M. Beg, A. Jain, F. Pierini, N. Gadegaard, R. Hogg, L. Manjakkal, J. Energy Storage 2023, 73, 108811.

[48] C. Rinoldi, Y. Ziai, S. S. Zargarian, P. Nakielski, K. Zembrzycki, M. A. H. Bayan, A. B. Zakrzewska, R. Fiorelli, M. Lanzi, A. Kostrzewska- Ksie˛yk, R. Czajkowski, E. Kublik, L. Kaczmarek, F. Pierini, ACS Appl. Mater. Interfaces 2023, 15, 6283.

[49] M. Alfatama, Y. Shahzad, H. Choukaife, Adv. Colloid Interface Sci.

2024, 325, 103098.

[50] H. Turasan, M. Cakmak, J. Kokini, J. Mater. Sci. 2019, 54, 8872.

[51] Y. F. Chen, Y. C. Lee, J. C. M. Lee, J. W. Li, C. W. Chiu, Adv. Compos. Hybrid Mater. 2024, 7, 1.

[52] A. Gadeval, N. Anup, B. Pawar, S. Mule, S. Otavi, R. Sahu, R. Kumar Tekade, Int. J. Pharm. 2024, 667, 124882.

[53] X. Cao, A. Mohamed, S. H. Gordon, J. L. Willett, D. J. Sessa, Ther- mochim. Acta 2003, 406, 115.

[54] M. Hassan, M. Sulaiman, P. D. Yuvaraju, E. Galiwango, I. U. Rehman,

A. H. Al-Marzouqi, A. Khaleel, S. Mohsin, J. Funct. Biomater. 2022, 13, 13.

[55] Ł. Kaniuk, U. Stachewicz, ACS Biomater. Sci. Eng. 2021, 7, 5339.

[56] S. Metwally, S. Ferraris, S. Spriano, Z. J. Krysiak, Ł. Kaniuk, M. M. Marzec, S. K. Kim, P. K. Szewczyk, A. Gruszczyn´ski, M. Wytrwal-Sarna,

J. E. Karbowniczek, A. Bernasik, S. Kar-Narayan, U. Stachewicz, Mater. Des. 2020, 194, 108915.

[57] A. Kosik-Kozioł, P. Nakielski, D. Rybak, W. Fra˛czek, C. Rinoldi, M. Lanzi, M. Grodzik, F. Pierini, ACS Appl. Mater. Interfaces 2024, 16, 32128.